Team Third

Curtis Dunford
ATLS / MCEN 4151 001
Dr. Sunberg
Nov 17, 2025
CU Boulder College of Engineering

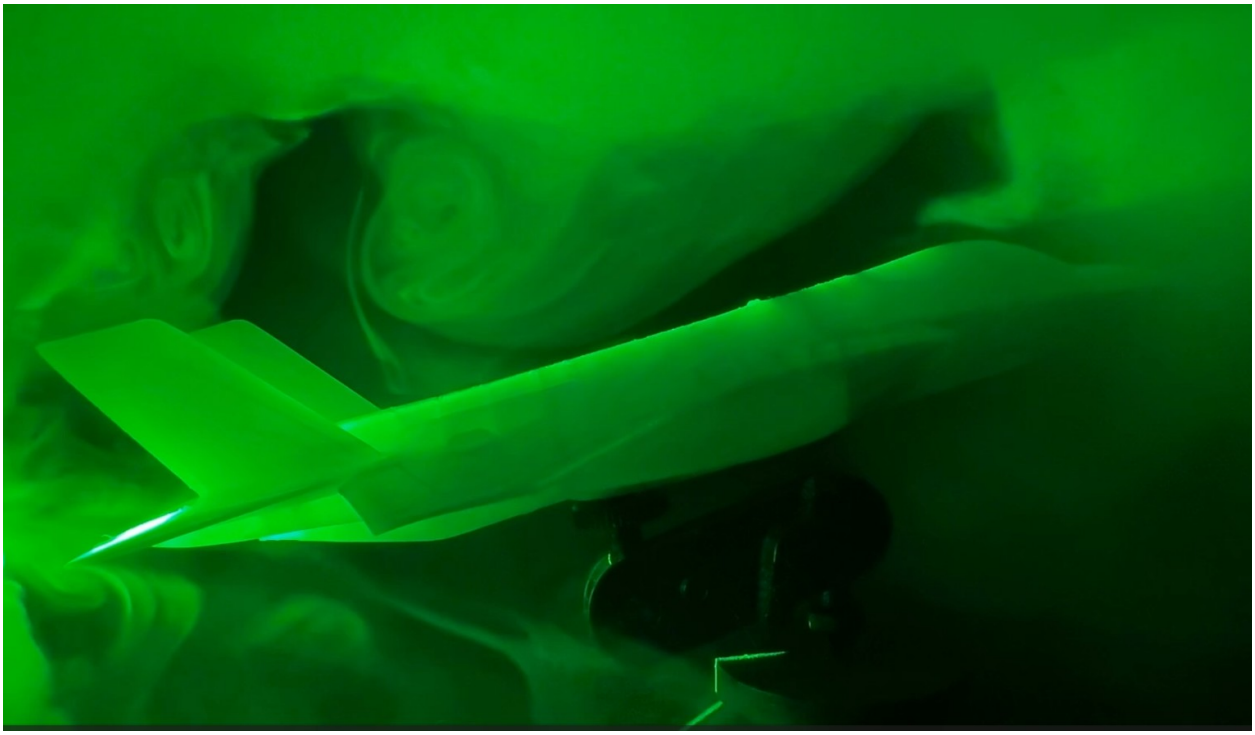

Figure 1: Seeded vortex cores whirl in the low pressure induced vortex lift region

Abstract

This project investigates vortex driven lift in delta fighter aerodynamics using a custom dual plane laser visualization system. My team and I assembled the first version of a homemade wind tunnel, but the early images were dominated by fog scatter and recirculation instead of showing the true leading edge vortex. After reviewing these initial images and video, I refined the apparatus on my own by rebuilding sections of the tunnel, stabilizing the inflow, and repositioning the perpendicular laser sheets so that they would illuminate the planform from behind, in the direction opposite to the direction of seeded flow.

Experimental Setup and Methods

My team and I built the first version of the homemade wind tunnel together during an early session. This initial box established the basic enclosure and mounting geometry for the delta wing model, but early tests revealed strong recirculation zones and non uniform fog distribution that obscured the leading edge vortex. After collecting this preliminary dataset, I continued developing the setup on my own. I rebuilt sections of the tunnel interior, smoothed surfaces, and added simple flow conditioning so that the fog entered the test section with a more uniform distribution and the vortex could form consistently at the chosen angle of attack.

Before constructing the optical system, I sketched the planned dual plane beam layout on a chalkboard, including approximate sheet heights and intended illumination regions around the model. To understand how laser beams spread and how sheet like illumination forms, I reviewed the application note Laser Beam Shaping Overview from Edmund Optics [1], which is recommended on the FlowViz website.[4] This resource helped me interpret beam behavior in the tight geometry of the tunnel. Instead of shaping beams manually with lenses, I used compact laser modules bought on Amazon that include built in beam shapers which flatten and widen the beam into a usable sheet directly from the housing. The chosen wavelength for the experiment was 520nm, resulting in a highly visible green hue.

To mount and align the lasers, I modeled a small optical cube in Autodesk Fusion 360, then printed it in carbon fiber reinforced PETG (polyethylene terephthalate glycol). This custom cube allows one to three laser modules to be mounted in line to produce parallel illumination planes, or a single module to be placed at different vertical heights to create cross section sheets at various locations. The cube attaches to a small optical breadboard that I built to secure the lasers and provide stable alignment. Using this system, I oriented one sheet so it passed through the vortex core and a second sheet so it illuminated the outer circulation region.

The delta-wing fighter model was printed in glow-in-the-dark PLA filament. Before the main run, I tested a sample in front of the laser aperture and saw a strong, uniform phosphorescent response, confirming that the material would clearly reveal where the beam intersected the model and surrounding flow. Fog from a small consumer fog machine was introduced upstream of the test region and allowed to mix before entering the illuminated section of the tunnel. After adjusting the internal geometry and flow conditioning, the tracer density became more uniform and the vortex structure appeared consistently during runs. This refined configuration provided the necessary flow quality for visualizing the vortex driven lift phenomenon.

Imaging Setup and Post Processing

I first shot the early tests using my Canon EOS R50, but the camera struggled with this particular setup. The strong contrast between the bright laser sheets and the dark interior of the tunnel caused the autofocus system to hunt, and the limited depth of field at close range made it difficult to keep both laser planes and the wing in focus at the same time. Even with manual adjustments, the exposure tended to clip the illuminated fog particles while underexposing the surrounding flow field.

Because of these limitations, I switched to the iPhone 16 Pro Max and recorded the sequences in slow motion at 120 frames per second. The phone's high resolution stacked sensor and naturally deep depth of field kept the entire illuminated region sharp without constant refocusing. Its adaptive exposure system was able to lock onto the illuminated fog particles as they moved through the sheets, maintaining clear visibility of the vortex core and shear layer. Apple's Photonic Engine and Computational Imaging stack with Deep Fusion excels in lowlight imaging. The fast readout and high frame rate reduced motion blur and rolling shutter effects, producing more stable and usable footage than the mirrorless camera. For this experiment the iPhone provided the most reliable imaging performance and became the main capture device.

Seeded Tunnel Flow

Reynolds number estimate for the seeded tunnel flow

To characterize the flow regime around the delta planform, we estimate a chord-based Reynolds number using the nominal fan rating and measured test-section dimensions.

The axial fan is rated at

$$Q = 100 \text{ cfm} = 100 \text{ ft}^3/\text{min}.$$

Using 1 ft = 0.3048 m, the volumetric flow rate in SI units is

$$1 \text{ ft}^3 = (0.3048 \text{ m})^3 \approx 0.0283168 \text{ m}^3,$$

$$Q = 100 \times 0.0283168 \approx 2.83 \text{ m}^3/\text{min} = \frac{2.83}{60} \approx 4.72 \times 10^{-2} \text{ m}^3/\text{s}.$$

The test section has a rectangular cross section with width $W = 141$ mm $= 0.141$ m and height $H = 175$ mm $= 0.175$ m, giving an area

$$A = WH = 0.141 \times 0.175 \approx 2.47 \times 10^{-2} \text{ m}^2.$$

Assuming incompressible steady flow, the mean tunnel speed is

$$U \approx \frac{Q}{A} = \frac{4.72 \times 10^{-2}}{2.47 \times 10^{-2}} \approx 1.9 \text{ m/s}.$$

For external flow over a wing, the conventional Reynolds number is based on the chord length,

$$Re_c = \frac{\rho U_\infty c}{\mu},$$

where c is the chord, U_∞ is the freestream velocity, and ρ and μ are the density and dynamic viscosity of air. Here we take the model chord as

$$c = 51 \text{ mm} = 0.051 \text{ m},$$

and approximate the freestream as the mean tunnel speed $U_\infty \approx U$. Using standard room-temperature air properties, $\rho \approx 1.2$ kg/m^3 and $\mu \approx 1.8 \times 10^{-5}$ Pa·s, gives

$$Re_c = \frac{(1.2)(1.9)(0.051)}{1.8 \times 10^{-5}} \approx 6.5 \times 10^3.$$

Flow Phenomena

The double-delta shaped model used in this experiment is a low aspect ratio, highly swept wing–body configuration. Approximating the planform as rectangular with span $b \approx 0.132$ m and chord $c = 0.051$ m gives an aspect ratio

$$AR \approx \frac{b^2}{bc} \approx \frac{0.132^2}{0.132 \times 0.051} \approx 2.6,$$

which is typical of fighter-type delta wings [3]. From the previous section, the mean tunnel speed is about $U_\infty \approx 1.9$ m/s, giving a small Mach number $M \ll 0.3$ and a chord Reynolds number $Re_c \approx 6.5 \times 10^3$. Internally, the tunnel Reynolds number based on hydraulic diameter is an order of magnitude higher, so the core flow is turbulent, but the external flow over the small model is best described as a low-Re, vortex-dominated incompressible flow.

Tip vortices, downwash, and the lifting-line picture

In finite-wing aerodynamics the basic picture is that the wing carries a bound vortex along its span and sheds a sheet of trailing vorticity into the wake. The wing-tip vortices and the trailing vortex sheet induce a downward velocity (downwash) over the wing, which effectively tilts the local flow downward [3]. A section of the wing at spanwise position y sees an effective angle of attack

$$\alpha_{\text{eff}}(y) = \alpha(y) - \alpha_i(y),$$

where α is the geometric angle of attack and $\alpha_i = w/U_\infty$ is the induced angle due to the downwash velocity w [3]. This reduction in effective angle of attack lowers the lift-curve slope relative to the 2D airfoil value and introduces induced drag.

The downwash itself comes from the velocity field of the vortex system. For a directed element $d\vec{\ell}$ of a vortex filament with circulation Γ, the induced velocity at a point with position vector $\vec{r}$ measured from the filament is given by the Biot–Savart law

$$d\vec{V} = \frac{\Gamma}{4\pi} \frac{d\vec{\ell} \times \vec{r}}{|\vec{r}|^3}.$$

In Prandtl's lifting-line theory, the finite wing is replaced by a spanwise lifting line with circulation $\Gamma(y)$ and a vortex sheet that trails downstream from this line [3]. Integrating the Biot–Savart expression over the trailing vortex system leads to a spanwise distribution of downwash $w(y)$ and to Prandtl's fundamental lifting-line equation relating $\Gamma(y)$, $\alpha(y)$, and the local airfoil characteristics.

For an ideal elliptic circulation distribution, this integration yields a remarkably simple result: the downwash is constant along the span and can be written as

$$w = \frac{\Gamma_0}{2b},$$

where Γ_0 is the maximum bound circulation at the centerline [3]. In this special case, the induced angle of attack and induced drag coefficient become

$$\alpha_i = \frac{C_L}{\pi AR}, \qquad C_{D,i} = \frac{C_L^2}{\pi AR},$$

which are the classical finite-wing relations summarized in Anderson's chapter [3].

As an order-of-magnitude check for the present model, we borrow Anderson's approximate lift-curve slope for a sharp 60° delta wing, about 0.05 per degree of angle of attack [3]. At the experimental setting of $\alpha = 15°$, this suggests

$$C_L \approx 0.05 \times 15 \approx 0.75.$$

With $AR \approx 2.6$, the induced angle of attack predicted by lifting-line theory is

$$\alpha_i \approx \frac{C_L}{\pi AR} \approx \frac{0.75}{\pi \times 2.6} \approx 0.09 \text{ rad} \approx 5°.$$

The effective angle of attack seen by an attached-flow section would then be

$$\alpha_{\text{eff}} \approx \alpha - \alpha_i \approx 15° - 5° \approx 10°,$$

and the corresponding induced downwash velocity is $w \approx U_\infty \alpha_i \approx 0.18$ m/s. These numbers show that even a small tabletop wing in this regime bends the local flow downward by several degrees through its tip-vortex system, in line with the finite-wing picture developed in [3].

Circulation and the role of the leading-edge vortex

Locally, the lift per unit span is related to circulation by the Kutta–Joukowski relation

$$L'(y) = \rho U_\infty \Gamma(y).$$

For an elliptic circulation distribution the maximum centerline circulation Γ_0 is related to the total lift coefficient by

$$\Gamma_0 = \frac{2}{\pi} U_\infty c\, C_L,$$

obtained by integrating $L' = \rho U_\infty \Gamma(y)$ across the span and equating the result to $L = \frac{1}{2}\rho U_\infty^2 S C_L$ [3]. With $U_\infty \approx 1.9$ m/s, $c = 0.051$ m, and $C_L \approx 0.75$, we obtain

$$\Gamma_0 \approx \frac{2}{\pi}(1.9)(0.051)(0.75) \approx 4.6 \times 10^{-2} \text{ m}^2/\text{s}.$$

If the wing behaved like a polite elliptic wing with attached flow, this circulation would be distributed smoothly along the span, and the induced drag and downwash could be described entirely by lifting-line theory.

Our model does not behave that politely. The sharp double-delta leading edge at $\alpha = 15°$ forces early separation and the formation of a coherent leading-edge vortex (LEV) over the suction surface. Anderson's discussion of sharp delta wings emphasizes that this LEV produces a concentrated region of very low pressure near the leading edge and that a significant portion of the total circulation is associated with this vortex rather than with a thin attached boundary layer [3]. In other words, the bound circulation $\Gamma(y)$ required by Kutta–Joukowski is now carried partly by an attached-flow component and partly by the rolled-up leading-edge vortex.

The laser-sheet visualization makes this redistribution of circulation visible. The model outline marks the solid boundary. Just above the leading edge there is a darker, under-seeded region where the fog density drops; this corresponds to the low-density, low-pressure core of the LEV. Outside this core, a brighter fog layer wraps over the wing and bends downward toward the trailing edge, tracing the shear layer that separates from the leading edge and then rolls up around the vortex. In circulation language, the LEV is a concentrated vortex filament running roughly parallel to the leading edge, carrying a large fraction of the Γ needed to generate the measured lift, while the surrounding fog layer shows the induced flow field that Biot–Savart predicts for such a vortex element.

Shear-layer instability and unsteady structure

The leading-edge vortex in this experiment is not perfectly steady or conical. In the images, the outer fog layer around the dark suction core develops scalloped, wavy distortions and local spiral roll-up, especially in the thicker region above the wing. This behavior is consistent with shear-layer instabilities. The interface between the high-speed swirling flow inside the vortex core and the slower outer tunnel flow supports a strong velocity gradient, so small perturbations grow into Kelvin–Helmholtz-type waves and then roll up into secondary vortices.

From the Biot–Savart point of view, these secondary vortices are additional small vortex filaments superposed on the primary LEV and tip-vortex system. Each new filament contributes its own induced velocity field according to

$$d\vec{V} = \frac{\Gamma}{4\pi}\frac{d\vec{\ell}\times\vec{r}}{|\vec{r}|^3},$$

so the instantaneous flow is a superposition of the mean downwash, the primary LEV field, and the velocities induced by these smaller vortical structures. At the present low Reynolds number, the instabilities do not yet drive the primary vortex to full breakdown; instead, they appear as a breathing motion of the fog envelope and small vortical swirls riding on top of the main structure. This matches Anderson's description that sharp low-aspect-ratio wings at moderate angles of attack sit in a regime where a strong leading-edge vortex enhances lift, while unsteady shear-layer and vortex dynamics begin to develop as the angle of attack increases toward breakdown [3].

Overall, the flow field around the model combines the finite-wing tip-vortex and downwash mechanisms from classical lifting-line theory with an additional leading-edge vortex that carries a large share of the circulation and produces a strong suction peak over the front portion of the wing. The laser-sheet visualization captures both pieces of this story: the global bending of the flow associated with induced downwash and the concentrated swirling motion of the leading-edge vortex and its unstable shear layer.

To put an actual number on the Biot–Savart estimate, we approximate the leading-edge vortex as a straight vortex filament running above the wing. For a long straight filament, the induced tangential velocity at distance r from the core is

$$V_\theta(r) = \frac{\Gamma}{2\pi r}.$$

Using the circulation estimate from above, $\Gamma \approx \Gamma_0 \approx 4.6\times10^{-2}$ m^2/s, and a representative distance $r = 0.03$ m from the core to the outer bright fog layer, we obtain

$$V_\theta(0.03) = \frac{4.6\times10^{-2}}{2\pi(0.03)} \approx 2.4\times10^{-1} \text{ m/s}.$$

Closer to the core, at $r = 0.02$ m and $r = 0.015$ m, the same expression gives

$$V_\theta(0.02) \approx 3.7 \times 10^{-1} \text{ m/s}, \qquad V_\theta(0.015) \approx 4.9 \times 10^{-1} \text{ m/s}.$$

Thus the swirl velocities predicted by the Biot–Savart law are on the order of 0.25–0.5 m/s, roughly 10–25% of the mean tunnel speed $U_\infty \approx 1.9$ m/s. These values are fully consistent with the strong curvature of the fog sheet and the tight rolling motion observed in the images: the leading-edge vortex is not a gentle perturbation but a substantial rotational core superposed on the mean flow.

Conclusion

In the images, the bright fog layer that wraps around the darker core exhibits a scalloped, wavy outer boundary and inside the low pressure vortex region below, it occasionally rolls up into smaller vortical structures. This layer represents the shear layer separating the high speed, swirling flow inside the vortex core from the slower, more uniform outer tunnel flow. A strong velocity jump across such a layer is susceptible to Kelvin Helmholtz type instabilities, in which small perturbations grow into waves and then roll up into secondary vortices.

At $Re_c \approx 6.5 \times 10^3$, these shear layer instabilities do not yet destroy the coherence of the main leading edge vortex; instead, they appear as gentle dancing of the fog envelope. Anderson notes that, as angle of attack increases on sharp delta wings, the leading edge vortices can eventually undergo breakdown, accompanied by large scale oscillations of the breakdown location and loss of the concentrated suction peak [3]. The fluctuating, wavy interface of the fog layer seen here can be interpreted as an early manifestation of the same family of unsteady vortex phenomena. The primary vortex remains intact and continues to provide strong suction and vortex lift over the wing, but its surrounding shear layer is already dynamically active, continuously rolling up and shedding smaller vortical structures that ride downstream over the model.

Anderson reports that for a sharp 60° delta wing the lift curve slope is modest, on the order of 0.05 per degree of angle of attack, and that lift continues to increase to relatively large angles before stall, with stall angles on the order of 35° and maximum lift coefficients around $C_{L,\max} \sim 1.3$ for subsonic flow [3]. Our operating point, $\alpha = 15°$, lies in the approximate middle of this pre breakdown regime. Although the low Reynolds number and geometric differences between the textbook delta and our modern fighter planform, means that the exact $C_L(\alpha)$ curve is not directly comparable. However, the qualitative picture is the same: a sharp, highly swept wing supports stable leading edge vortices that produce strong suction peaks near the leading edges and significantly augment the lift.

Beyond the fluid mechanics, this project highlighted the iterative and collaborative nature of experimental flow visualization. Working with my teammates Isaac and Cooper, we systematically explored the tunnel geometry, model mounting, seeding rate, and laser alignment to obtain images in which the leading edge vortex and its surrounding shear layer were unambiguous. Many early configurations produced either washed out images or flows that were too weakly seeded to interpret, and only through repeated adjustment of each subsystem did the final, clear visualization emerge.

References

Edmund Optics, "Laser Beam Shaping Overview," Application Note, https://www.edmundoptics.com/knowledge-center/application-notes/optics/laser-beam-shaping-overview/, accessed November 20, 2025.

R. W. Fox, A. T. McDonald, and P. J. Pritchard, *Fox and McDonald's Introduction to Fluid Mechanics*, 8th ed., John Wiley & Sons, Hoboken, NJ, 2009.

J. D. Anderson, *Fundamentals of Aerodynamics*, 2nd ed., McGraw Hill, New York, 1991.

Flow Visualization Course, "FlowVis.org – The Physics and Art of Fluid Flow," University of Colorado Boulder, 2025. https://www.flowvis.org/.

C. Tropea, A. L. Yarin, and J. F. Foss (eds.), *Springer Handbook of Experimental Fluid Mechanics*, Springer, Berlin, 2007.

Appendix

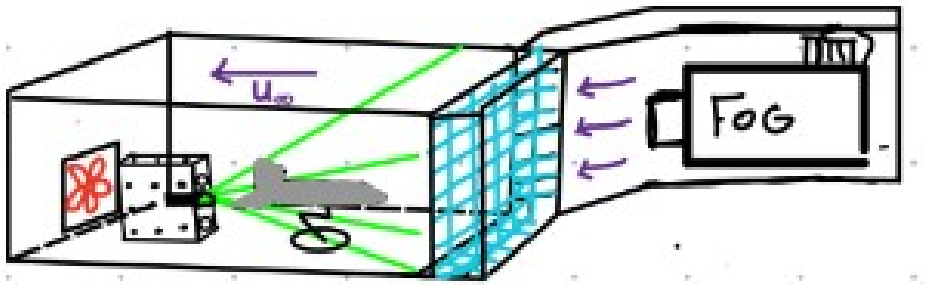

Figure 2: Experimental setup

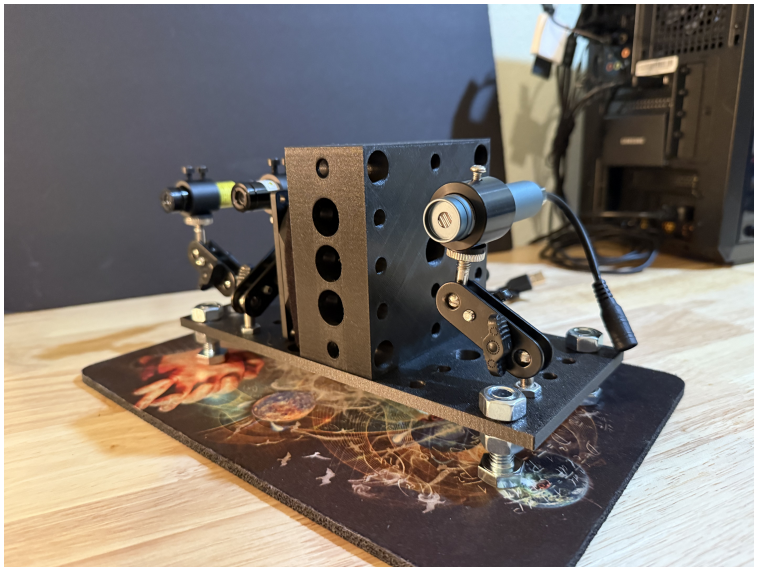

Figure 3: Laser Apertures and Mounting System

Figure 4: 3D Printed delta model in glow PLA